Journal of
Computational and Theoretical Nanoscience
Vol. 5, 690–703, 2008

Equivalent Circuit (EC) FDTD Method for the Modeling of Surface Plasmon Based Couplers

A. Rennings[1, 3, *], J. Mosig[1, 3], C. Caloz[2], D. Erni[3], and P. Waldow[1]

[1] *IMST GmbH, D-47475 Kamp-Lintfort, Germany*
[2] *Poly-Grames Research Center, École Polytechnique de Montréal, Montréal, H3T 1J4, Québec, Canada*
[3] *General and Theoretical Electrical Engineering, University of Duisburg-Essen, D-47048 Duisburg, Germany*

An equivalent circuit (EC) FDTD method is derived, first for the case of non-dispersive materials and next for the case of dispersive materials. In the later case, both an extended-Drude and a combined Drude/1-pole Lorentz permittivity function, with corresponding circuit (admittance) models, are proposed and shown to perfectly agree with experimental data over a wide range of frequencies, with a broader frequency range of validity for the second model. A novel optical nano-coupler based on surface plasmon (SP) coupling between two metal-dielectric interfaces of a metal (Ag) slab embedded in a dielectric material (SiO_2) is proposed, analyzed with the EC FDTD method, characterized in terms of scattering parameters and fields distributions, and shown to provide several operation modes, including power splitter and diplexer. The structure features super-compact size (around 2 μm) and low-loss (0.4 dB at 769 nm for power splitting operation, and 1.4 dB and 2.4 dB for the diplexing of light waves in 633 nm and 533 nm bands), and may therefore find various applications.

Keywords: FDTD, Equivalent Circuit (EC), Dispersive Media, Surface Plasmon (SP), Nano-Scale Device, Co-Directional Coupler, Diplexer, Power Splitter, Integrated Optics.

1. INTRODUCTION

Recently, there has been a regain of interest in surface plasmons (SPs) (e.g., Refs. [1, 2]) due to the fact that their spectacular wavelength compression capability and their technological realizability represent unprecedented opportunities for novel nano-scale optical applications.[3–5]

SPs are electron plasma density oscillations bound as a surface wave to a metal/dielectric interface. They are fundamentally dispersive waves due the permittivity dispersion of the metal used (in conjunction with dielectric) to support them. A proper analysis of SP structures requires therefore a computational approach capable of accurately accounting for the dispersion effects, which are generally of Drude type to the first order.

This paper presents an equivalent circuit (EC) finite difference time domain (FDTD)[8, 9] method for general dispersive media, which applies in particular to the case of SP structures. In addition, it proposes a novel optical nano-coupler based on SP coupling between the two metal-dielectric interfaces of a metal slab embedded in a dielectric material, which is analyzed by EC FDTD.

*Author to whom correspondence should be addressed.

2. EC FDTD METHOD

This section presents the equivalent circuit (EC) FDTD method used for the analysis of the proposed SP-coupled couplers. Section 2.1 introduces a compact notation based on a spatial-shift operator, Section 2.2 derives in this notation the fundamental update relations for non-dispersive materials, and Section 2.3 extends these relations to the case of dispersive materials, such as metals in the optical regime.

2.1. Notation of the Discrete Calculus

All operators, including matrices, are denoted by upright capital letters (e.g., S) and vectors are denoted by italic bold characters (vector field $\boldsymbol{E}$). The following describes more specific aspects of the notation.

(1) *Discrete Fields*: The six space-continuous scalar field components of the form $F_{\mathrm{cont}}(\boldsymbol{x}, t), \boldsymbol{x} \in \mathbb{R}^3, t \in \mathbb{R}$ of the electromagnetic field are represented by six *discrete fields* of the form $F^n_{\mathrm{disc}}(\boldsymbol{X}), \boldsymbol{X} \in \mathbb{Z}^3, n \in \mathbb{Z}$, where $\boldsymbol{X}$ is the three-dimensional spatial index vector and n is the time index. The index vector $\boldsymbol{X}$ is usually implicit [F^n_{disc} and not $F^n_{\mathrm{disc}}(\boldsymbol{X})$], since it is assumed that all discrete fields depend on $\boldsymbol{X}$. In contrast, the time index n is always mentioned

 1546-1955/2008/5/690/014 doi:10.1166/jctn.2008.040

explicitly for the time discrete case (conventional FDTD notation with upper index).

(2) *Modulo-Three Notation and Variable Indices*: For the sake of notational simplicity and compactness, the component and spatial direction indices are numbered in a modulo-three sense, [e.g., $F_0 \equiv F_x, F_1 \equiv F_y, F_2 \equiv F_z$ and $F_3 \equiv F_0, F_4 \equiv F_1$, etc.], i.e., the effective index is always an element of the set $\{0, 1, 2\}$. In 3D figures the direction indices $d \in \{0, 1, 2\}$ are explicitly given (as absolute numbers), whereas in 2D figures (projections of a 3D arrangement along the Cartesian axes) the variable indices $(d, d+1, d+2)$ are used. By assigning $\{0, 1, 2\}$ to d one gets the projection onto a desired plane. The variable indices are also utilized to specify vectorial equations in a scalar manner, where a specific component is obtained by assigning $\{0, 1, 2\}$ to d.

(3) *Discrete Spatial-Shift Operators*: In finite difference schemes the application of spatial operators onto discrete fields is usually specified by index changes along with appropriate weighting factors, which often results in cumbersome equations. In order to eliminate this inconvenience, we introduce the shift operator S_d and its inverse S_d^{-1}. Together with the null and the identity element these shift operators generate an operator space $\mathbb{O}$, which in algebraic terms is called a *commutative ring*. The shift operators are defined via their action onto the discrete fields:

$$\begin{aligned} \mathrm{S}_d F(\boldsymbol{X}) &= F(\boldsymbol{X} + \boldsymbol{U}_d), \\ \left\{\mathrm{S}_d^{-1} + \mathrm{S}_{d+1}\right\} F(\boldsymbol{X}) &= F(\boldsymbol{X} - \boldsymbol{U}_d) + F(\boldsymbol{X} + \boldsymbol{U}_{d+1}) \end{aligned} \tag{1}$$

with the index unit vectors $\boldsymbol{U}_0 = (1, 0, 0)^{\mathrm{T}}$, $\boldsymbol{U}_1 = (0, 1, 0)^{\mathrm{T}}$ and $\boldsymbol{U}_2 = (0, 0, 1)^{\mathrm{T}}$. The application of S_d onto a field not depending on X_d yields the field unchanged (identity operation). The effect of successive operators (multiplication in $\mathbb{O}$) is illustrated in the following example:

$$\begin{aligned} \mathrm{S}_d \alpha \mathrm{S}_{d+2}^{-1} F(\boldsymbol{X}) &= \alpha \mathrm{S}_d \mathrm{S}_{d+2}^{-1} F(\boldsymbol{X}) = \mathrm{S}_{d+2}^{-1} \mathrm{S}_d \alpha F(\boldsymbol{X}) \\ &= \alpha F(\boldsymbol{X} + \boldsymbol{U}_d - \boldsymbol{U}_{d+2}) \quad \text{with } \alpha \in \mathbb{R} \end{aligned} \tag{2}$$

2.2. Basic EC FDTD for Non-Dispersive Materials

The basic EC FDTD scheme is derived from an approximation of Maxwell's equations in integral form, including electric losses σ_e, magnetic losses σ_m, and a current density source $\boldsymbol{J}_{\mathrm{src}}$ (soft excitation),

$$\oint_{\partial A} \boldsymbol{H} \cdot \mathrm{d}\boldsymbol{\ell} = +\frac{\mathrm{d}}{\mathrm{d}t} \iint_A \varepsilon \boldsymbol{E} \cdot \mathrm{d}\boldsymbol{A} + \iint_A \sigma_{\mathrm{e}} \boldsymbol{E} \cdot \mathrm{d}\boldsymbol{A} - \iint_A \boldsymbol{J}_{\mathrm{src}} \cdot \mathrm{d}\boldsymbol{A} \tag{3}$$

$$\oint_{\partial A} \boldsymbol{E} \cdot \mathrm{d}\boldsymbol{\ell} = -\frac{\mathrm{d}}{\mathrm{d}t} \iint_A \mu \boldsymbol{H} \cdot \mathrm{d}\boldsymbol{A} - \iint_A \sigma_{\mathrm{m}} \boldsymbol{H} \cdot \mathrm{d}\boldsymbol{A} \tag{4}$$

where all material constitutive parameters $(\varepsilon, \mu, \sigma_{\mathrm{e}}, \sigma_{\mathrm{m}})$ are considered *non-dispersive*, i.e., independent of frequency (but possibly inhomogeneous).

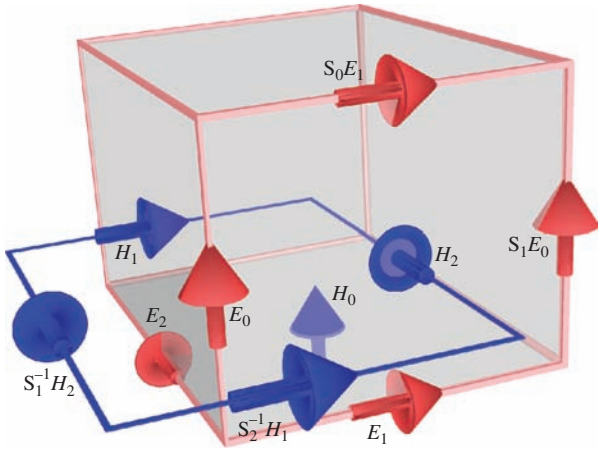

Fig. 1. Yee cell, which consists of a *main mesh* subcell (parallelepipedic structure in the figure) and a *dual mesh* subcell (staggered parallelepipedic structure, of which only one face is shown in the figure). The Yee cell includes six unshifted field samples. Additionally four positively or negatively shifted field samples are shown, which are required for the approximation of Eqs. (3) and (4).

These space-time continuous equations are *spatially discretized* using the well-known *Yee cell*,[6] which is depicted in Figure 1. Within the Yee cell, the electric field is sampled at the edges of the main mesh subcell while the magnetic field is sampled at the edges of the dual mesh subcell. The field samples within the Yee cell are located by the index vector $\boldsymbol{X} = (X_0, X_1, X_2)^{\mathrm{T}}$, according to the notations of Section 2.1.

The Yee discretization details of the proposed EC FDTD formulation are shown in Figure 2. The magnetic field samples are located normally at the *center* of the faces of the main mesh subcells and are *symmetrically surrounded* by four adjacent tangential electric field samples. In contrast, for a non-uniform mesh, the electric field samples are *not* located symmetrically with respect to the surrounding magnetic field samples. In this scheme both the electric *and the magnetic* material parameters are approximated by *main mesh "blocks" with piecewise constant constitutive parameters*,[a] which allows a natural meshing of inhomogeneous materials, since a changes in the material parameters typically occur at the boundaries of objects.

In the case of a non-uniform mesh, the dimensions of the mesh cells vary across space, and the cell edge length Δ_d is only a function of the component X_d of the index vector $\boldsymbol{X}$. According to the notations of Section 2.1, the dimensions of the dual mesh subcell, $\overline{\Delta}_d$, are related to the dimensions of the main mesh subcell, Δ_d, by

$$\overline{\Delta}_d = \frac{1}{2}\left(\mathrm{S}_d^{-1}\Delta_d + \Delta_d\right) = \frac{1}{2}\left\{\mathrm{S}_d^{-1} + 1\right\}\Delta_d \quad \forall d \in \{0, 1, 2\} \tag{5}$$

[a]Conventionally, the magnetic material parameters are approximated by *dual mesh* blocks with piecewise constant constitutive parameters.[6]

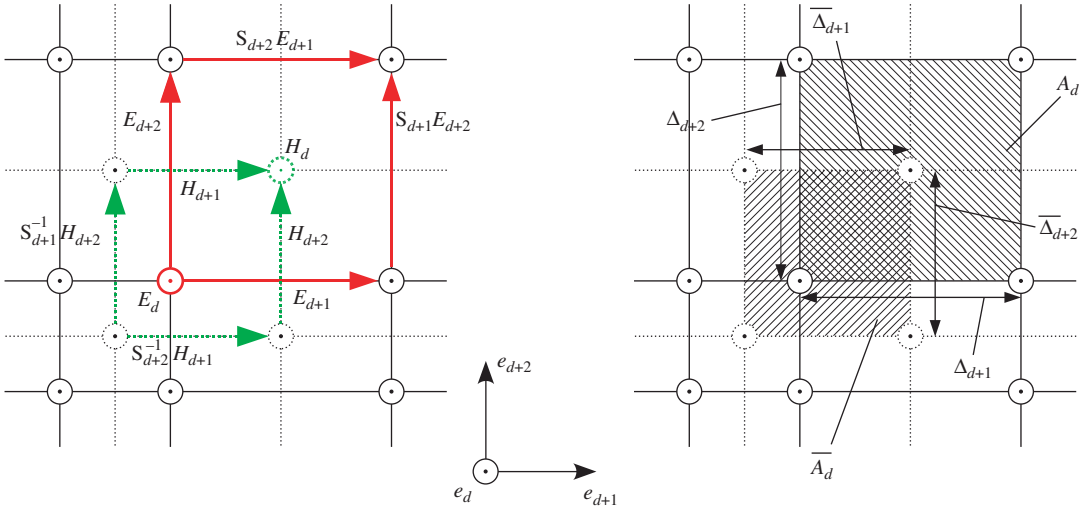

Fig. 2. Details of the Yee cell (Fig. 1) discretization. Used components and corresponding subcell dimensions for the spatial discretization of Eqs. (3) and (4) leading to Eqs. (6) and (7).

Evaluating Maxwell's Eqs. (3) and (4) on all the faces of the main and dual mesh subcells, as represented in Figure 2, yields the (still time-continuous) spatially discretized generic equations

$$\oint_{\partial\overline{A}_d} \boldsymbol{H}\cdot\mathrm{d}\boldsymbol{\ell} \approx \left\{1-\mathrm{S}_{d+1}^{-1}\right\}H_{d+2}\overline{\Delta}_{d+2} - \left\{1-\mathrm{S}_{d+2}^{-1}\right\}H_{d+1}\overline{\Delta}_{d+1}$$

$$= +\frac{1}{4}\left\{1+\mathrm{S}_{d+1}^{-1}+\mathrm{S}_{d+2}^{-1}+\mathrm{S}_{d+1}^{-1}\mathrm{S}_{d+2}^{-1}\right\} \times\left[\varepsilon\Delta_{d+1}\Delta_{d+2}\right]\frac{1}{\Delta_d}\frac{\mathrm{d}}{\mathrm{d}t}E_d\Delta_d$$

$$+\frac{1}{4}\left\{1+\mathrm{S}_{d+1}^{-1}+\mathrm{S}_{d+2}^{-1}+\mathrm{S}_{d+1}^{-1}\mathrm{S}_{d+2}^{-1}\right\} \times\left[\sigma_\mathrm{e}\Delta_{d+1}\Delta_{d+2}\right]\frac{1}{\Delta_d}E_d\Delta_d - \overline{\Delta}_{d+1}\overline{\Delta}_{d+2}J_d^{\mathrm{src}}$$

$$\approx \iint_{\overline{A}_d}\ldots\cdot\,\mathrm{d}\boldsymbol{A} \qquad (6)$$

$$\oint_{\partial A_d} \boldsymbol{E}\cdot\mathrm{d}\boldsymbol{\ell} \approx \left\{\mathrm{S}_{d+1}-1\right\}E_{d+2}\Delta_{d+2} - \left\{\mathrm{S}_{d+2}-1\right\}E_{d+1}\Delta_{d+1}$$

$$= -\frac{\Delta_{d+1}\Delta_{d+2}}{\frac{1}{2}\left\{1+\mathrm{S}_d^{-1}\right\}\left[\frac{\Delta_d}{\mu}\right]}\frac{\mathrm{d}}{\mathrm{d}t}H_d\overline{\Delta}_d$$

$$-\frac{\Delta_{d+1}\Delta_{d+2}}{\frac{1}{2}\left\{1+\mathrm{S}_d^{-1}\right\}\left[\frac{\Delta_d}{\sigma_\mathrm{m}}\right]}H_d\overline{\Delta}_d \approx \iint_{A_d}\ldots\cdot\,\mathrm{d}\boldsymbol{A} \qquad (7)$$

where the fluxes $\iint_{\overline{A}d}\{\varepsilon,\sigma_\mathrm{e}\}\boldsymbol{E}\cdot\mathrm{d}\boldsymbol{A}$ on each face $\overline{A}_d$ (Fig. 2) through the *dual* mesh subcells have been approximated in Eq. (6). The *magnetic* parameters are constant in each A_d—transversal direction (where A_d is defined by the directions $d+1$ and $d+2$, Fig. 2, right) of the *main* mesh subcells, and therefore no useful averaging quantity may defined from the fluxes $\iint_{A_d}\{\mu,\sigma_\mathrm{m}\}\boldsymbol{H}\cdot\mathrm{d}\boldsymbol{A}$. In contrast, two different magnetic materials may exist in the longitudinal direction (d), and therefore the *effective magnetic* parameters may be approximated by averaging the magneto-motive force[b] $H_d\overline{\Delta}_d$

$$H_d\overline{\Delta}_d = B_d\frac{1}{2}\left\{1+\mathrm{S}_d^{-1}\right\}\left[\frac{\Delta_d}{\mu}\right] \doteq \frac{\mathrm{B}_d}{\mu_{d,\,\mathrm{eff}}}\overline{\Delta}_d$$

from which follows

$$\mu_{d,\,\mathrm{eff}}H_d = \frac{\overline{\Delta}_d}{\frac{1}{2}\left\{1+\mathrm{S}_d^{-1}\right\}\left[\frac{\Delta_d}{\mu}\right]}H_d \qquad (8)$$

The later product has been used in Eq. (7). The loss term $\sigma_{d,\,\mathrm{eff}}^{\mathrm{m}}H_d$ is evaluated in the same manner.

The products $E_d\Delta_d \doteq v_d$ in Eqs. (6) and (7) may be interpreted as the electric voltages along the edges of the main mesh subcells and the terms $H_d\overline{\Delta}_d \doteq i_d$ may be interpreted as the "magnetic voltages" along the edges of the dual mesh subcells.[c] This circuit analogy and inspection of Eqs. (6) and (7) naturally lead to the definition of the equivalent *lumped elements*

$$C_d = \frac{1}{4}\left\{1+\mathrm{S}_{d+1}^{-1}+\mathrm{S}_{d+2}^{-1}+\mathrm{S}_{d+1}^{-1}\mathrm{S}_{d+2}^{-1}\right\}\left[\varepsilon\Delta_{d+1}\Delta_{d+2}\right]\frac{1}{\Delta_d} \qquad (9)$$

$$G_d = \frac{1}{4}\left\{1+\mathrm{S}_{d+1}^{-1}+\mathrm{S}_{d+2}^{-1}+\mathrm{S}_{d+1}^{-1}\mathrm{S}_{d+2}^{-1}\right\}\left[\sigma_\mathrm{e}\Delta_{d+1}\Delta_{d+2}\right]\frac{1}{\Delta_d} \qquad (10)$$

which are interpreted as the local capacitance and conductance, and

$$L_d = \frac{\Delta_{d+1}\Delta_{d+2}}{\frac{1}{2}\left\{1+\mathrm{S}_d^{-1}\right\}\left[\frac{\Delta_d}{\mu}\right]}, \quad R_d = \frac{\Delta_{d+1}\Delta_{d+2}}{\frac{1}{2}\left\{1+\mathrm{S}_d^{-1}\right\}\left[\frac{\Delta_d}{\sigma_\mathrm{m}}\right]} \qquad (11)$$

[b]The magnetic flux density B_d is continuous here.

[c]Alternatively, the term $H_d\overline{\Delta}_d \doteq i_d$ can be interpreted as corresponding loop current in the face A_d of the main mesh cell (Fig. 3), which is related to the orthogonal magnetic field H_d component by the right-hand rule.

which are interpreted as the local inductance and resistance. To complete the circuit analogy, a lumped current source i_d^{src} is defined as

$$i_d^{\mathrm{src}} = \frac{1}{4}\left\{1+\mathrm{S}_{d+1}^{-1}+\mathrm{S}_{d+2}^{-1}+\mathrm{S}_{d+1}^{-1}\mathrm{S}_{d+2}^{-1}\right\}\left[\Delta_{d+1}\Delta_{d+2}\right]J_d^{\mathrm{src}} \quad (12)$$

With these local lumped elements Ampere's (3) and Faraday's (4) laws take the very compact EC form

$$\left\{1-\mathrm{S}_{d+1}^{-1}\right\}i_{d+2}-\left\{1-\mathrm{S}_{d+2}^{-1}\right\}i_{d+1}+i_d^{\mathrm{src}} = +C_d\frac{\mathrm{d}}{\mathrm{d}t}v_d+G_d v_d \quad (13)$$

$$\left\{\mathrm{S}_{d+1}-1\right\}v_{d+2}-\left\{\mathrm{S}_{d+2}-1\right\}v_{d+1} = -L_d\frac{\mathrm{d}}{\mathrm{d}t}i_d-R_d i_d \quad (14)$$

For each $d \in \{0,1,2\}$ Eq. (13) represents the Kirchhoff's current law for a current node and Eq. (14) represents the Kirchhoff's voltage law for a voltage loop. This "circuitization" of the Yee FDTD discretization of space may be represented by the 3D equivalent circuit cell shown in Figure 3.

The final step in the derivation of the EC FDTD scheme consists in *time-discretizing* the previous equations by using finite differences in order to set up the update equations. Defining a time step Δt and using the traditional leap-frog scheme, the voltage values are sampled at time multiples of Δt while the current values are sampled between these instances, i.e., at odd multiples of $\Delta t/2$. This leads to

$$\left\{1-\mathrm{S}_{d+1}^{-1}\right\}i_{d+2}^{n-1/2}-\left\{1-\mathrm{S}_{d+2}^{-1}\right\}i_{d+1}^{n-1/2}+i_{\mathrm{src},d}^{n-1/2} = +C_d\frac{v_d^n-v_d^{n-1}}{\Delta t}+G_d\frac{v_d^n+v_d^{n-1}}{2} \quad (15)$$

$$\left\{\mathrm{S}_{d+1}-1\right\}v_{d+2}^n-\left\{\mathrm{S}_{d+2}-1\right\}v_{d+1}^n = -L_d\frac{i_d^{n+1/2}-i_d^{n-1/2}}{\Delta t}-R_d\frac{i_d^{n+1/2}+i_d^{n-1/2}}{2} \quad (16)$$

and solving these equations for the latest voltages v_d^n and currents $i_d^{n+1/2}$ yield the final EC FDTD update equations for a non-dispersive material region of the computational domain

$$v_d^n = \frac{1-\frac{\Delta t G_d}{2C_d}}{1+\frac{\Delta t G_d}{2C_d}}v_d^{n-1} + \frac{\Delta t}{C_d}\frac{\left\{1-\mathrm{S}_{d+1}^{-1}\right\}i_{d+2}^{n-1/2}-\left\{1-\mathrm{S}_{d+2}^{-1}\right\}i_{d+1}^{n-1/2}+i_{\mathrm{src},d}^{n-1/2}}{1+\frac{\Delta t G_d}{2C_d}} \quad (17)$$

$$i_d^{n+1/2} = \frac{1-\frac{\Delta t R_d}{2L_d}}{1+\frac{\Delta t R_d}{2L_d}}i_d^{n-1/2} - \frac{\Delta t}{L_d}\frac{\left\{\mathrm{S}_{d+1}-1\right\}v_{d+2}^n-\left\{\mathrm{S}_{d+2}-1\right\}v_{d+1}^n}{1+\frac{\Delta t R_d}{2L_d}} \quad (18)$$

The update scheme for the non-dispersive case given in Eqs. (17) and (18) may be shown[10,11] to follow the stability criterion

$$\Delta t_{\text{non-disp}} < \frac{2}{\max_{X\in\Omega,\,d\in\{0,1,2\}}\sqrt{\frac{1}{C_d}\left(\frac{4}{L_{d+1}}+\frac{4}{S_{d+2}^{-1}L_{d+1}}+\frac{4}{L_{d+2}}+\frac{4}{S_{d+1}^{-1}L_{d+2}}\right)}} \doteq \frac{2}{\max_{X\in\Omega,\,d\in\{0,1,2\}}\omega_{\text{non-disp},d}} \quad (19)$$

For an uniform mesh the relation $\Delta t_{\text{non-disp}} = \sqrt{3/4}\Delta t_{\text{CFL}} \approx 87\%\ \Delta t_{\text{CFL}}$ holds, where Δt_{CFL} is the conventional time step based on the Courant-Friedrich-Levy (CFL) condition.[6] However, in non-uniform (graded) meshes, where the smallest cell is adjacent to a larger one (with at least 33% longer edges), the EC-based criterion yields a larger time step. This improvement depends on the size-ratio of directly adjacent cells. For extreme meshing situations an improvement factor $\Delta t_{\text{non-disp}}/\Delta t_{\text{CFL}}$ of 10 can easily be achieved. The ordinary CFL criteria has been derived for an uniform mesh and a homogeneous material distribution, therefore it seems to be too conservative in highly graded meshes, since the smallest cell size has to be used in the formula.

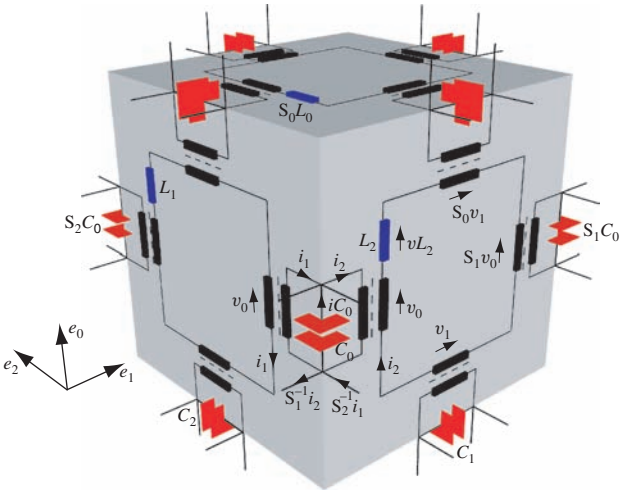

Fig. 3. 3D equivalent circuit cell for a non-dispersive and lossless material with (shunt) capacitances located at the edges of the main mesh cells (e-nodes) and (series) inductances (represented by the rectangle in the loop) located at the faces of the main mesh cells. The ideal 1:1-transformers are necessary to ensure a well defined loop current with a *one-to-one* correspondence to the orthogonal magnetic field component. The direction of the voltages v_d is positive in the parallel Cartesian direction $\boldsymbol{e}_d$ and the one for the loop currents i_d is positive with respect to the corresponding magnetic field component (right-hand rule). The values $i_{C_0} = C_0(\mathrm{d}/\mathrm{d}t)v_0$ and $v_{L_2} = L_2(\mathrm{d}/\mathrm{d}t)i_2$ are used as abbreviations within the figure.

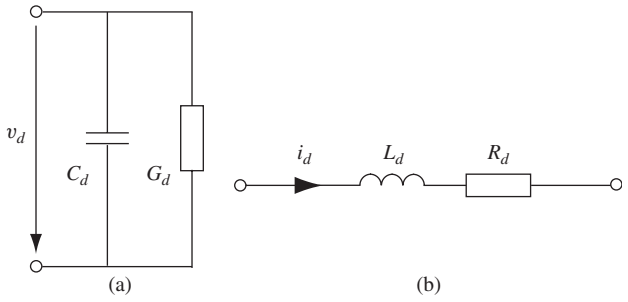

Fig. 4. Equivalent circuit models for non-dispersive and lossy media. (a) Shunt admittance $Y_{\text{non-disp}}$ located at E-field nodes (Fig. 3) and related to the non-dispersive $\varepsilon_{\text{non-disp}}$. (b) Series impedance $Z_{\text{non-disp}}$ located at H-field nodes (Fig. 3) and related to the frequency-independent $\mu_{\text{non-disp}}$.

2.3. Generalized EC Method for Dispersive Materials

Section 2.2 derived the basic EC FDTD scheme for *non-dispersive* materials. This has led to the emergence of the local admittance $Y_{\text{non-disp}} = \mathrm{j}\omega C \propto \mathrm{j}\omega\varepsilon_{\text{non-disp}}$ (Eq. (9)) constituted of a capacitance C with a parallel conductance G for loss (Eq. (9)) and a local impedance $Z_{\text{non-disp}} = \mathrm{j}\omega L \propto \mathrm{j}\omega\mu_{\text{non-disp}}$ (Eq. (11)) constituted of an inductance L with a series resistance R for loss, as represented in Figure 4, which are characteristic of non-dispersive media in the transmission line framework and correspond to the material non-dispersive constitutive parameters.

In this paper the EC FDTD scheme is applied to surface plasmonic waves (metal-based optics),[3] which involve metal with highly dispersive and lossy permittivity in the optical regime.[12] In order to handle such problems, we generalize the EC FDTD scheme to an *extended* EC scheme for dispersive materials. This extended scheme fundamentally consists in adding to the equivalent impedance $Z(\omega)$ and admittance $Y(\omega)$ the appropriate lumped elements to account for the specific dispersion relations considered, $\tilde{\mu}(\omega) \propto Z(\omega)/(\mathrm{j}\omega)$ and $\tilde{\varepsilon}(\omega) \propto Y(\omega)/(\mathrm{j}\omega)$. This transformation will require additional update equations. In general each inductor current and each capacitor voltage represents an update-value. Therefore our approach is comparable to the auxiliary differential equation (ADE) technique[7] in terms of memory requirements and computational effort.

The relation between the generalized dispersive admittance and the corresponding dispersive function $\tilde{\varepsilon}(\omega) = \varepsilon_\infty + \Delta\varepsilon'(\omega) - \mathrm{j}\sigma_\mathrm{e}/\omega - \mathrm{j}\varepsilon''(\omega)$, where $\varepsilon_\infty \doteq \tilde{\varepsilon}(\omega \to \infty)$, reads

$$\begin{aligned}\tilde{\varepsilon}_{d,\text{eff}} &= \frac{Y_d}{\mathrm{j}\omega}\frac{\Delta_d}{\overline{A}_d} \\ &= \frac{Y_d}{\mathrm{j}\omega}\frac{\Delta_d}{\frac{1}{4}\left\{1+\mathrm{S}_{d+1}^{-1}+\mathrm{S}_{d+2}^{-1}+\mathrm{S}_{d+1}^{-1}\mathrm{S}_{d+2}^{-1}\right\}\left[\Delta_{d+1}\Delta_{d+2}\right]} \\ &\doteq \frac{Y_d}{\mathrm{j}\omega\Delta_{\mathrm{e},d}}\end{aligned} \tag{20}$$

where $\Delta_{\mathrm{e},d}$ represents the form factor of an artificial subcell[d] with cross section $\overline{A}_d$ of the dual mesh and the height Δ_d of the main mesh, and has the dimension of a length. Similarly, the dispersive function $\tilde{\mu}(\omega) = \mu_\infty + \Delta\mu'(\omega) - \mathrm{j}\sigma_\mathrm{m}/\omega - \mathrm{j}\mu''(\omega)$ [where $\mu_\infty \doteq \tilde{\mu}(\omega \to \infty)$] can be determined from its corresponding generalized-dispersive impedance via

$$\tilde{\mu}_{d,\text{eff}} = \frac{Z_d}{\mathrm{j}\omega}\frac{\overline{\Delta}_d}{A_d} = \frac{Z_d}{\mathrm{j}\omega}\frac{\frac{1}{2}\left\{1+\mathrm{S}_d^{-1}\right\}\Delta_d}{\Delta_{d+1}\Delta_{d+2}} \doteq \frac{Z_d}{\mathrm{j}\omega\Delta_{\mathrm{m},d}} \tag{21}$$

where $\Delta_{\mathrm{m},d}$ represents the form factor of an artificial cell[e] with cross section A_d of the main mesh subcell and height $\overline{\Delta}_d$ of the dual mesh subcell.

3. TIME-DOMAIN EC MODELS FOR PLASMONIC METALS

This section presents two dispersive and lossy EC models for the *permittivity* of plasmonic metals, namely the *extended Drude model* and the *combined Drude/N-pole-Lorentz model*. The former is accurate up to the surface plasmon resonance frequency ω_{sp} (Ag–SiO_2 interface: $f_{\text{sp}} = 843$ THz, $\lambda_{\text{sp}} = 356$ nm), defined by $\Re\{\tilde{\varepsilon}_{\text{metal}}\}(\omega = \omega_{\text{sp}}) = -\varepsilon_{\text{insulator}}$, while the later has a range of validity extending above that surface resonance frequency up to the bulk plasma resonance ω_p (Ag: $f_\mathrm{p} = 922$ THz, $\lambda_\mathrm{p} = 325$ nm), defined by $\Re\{\tilde{\varepsilon}_{\text{metal}}\}(\omega = \omega_\mathrm{p}) = 0$, and also slightly above, as will be shown in the third part of this section.

3.1. Extended Drude EC Model

In the *extended Drude EC model* for metals, the EC admittance Y_d (in the direction d) includes an inductance $L_{\mathrm{D},d}$ with a series resistance $R_{\mathrm{D},d}$ in parallel with a capacitance C_d with a shunt conductance G_d, as shown in Figure 5(a), while the EC impedance Z_d is unchanged compared to the non-dispersive case (Fig. 4(b)) due to the non-magnetic nature ($\mu = \mu_0$) of the considered media. The constitutive parameters in Eqs. (20) and (21) become then, ignoring the index d for notational simplicity,

$$\begin{aligned}\tilde{\varepsilon}_{\text{Drude}} &= \frac{Y_{\text{Drude}}}{\mathrm{j}\omega\Delta_\mathrm{e}} = \frac{C}{\Delta_\mathrm{e}}\left\{1 - \frac{\frac{1}{L_\mathrm{D}C}}{\omega\left(\omega - \mathrm{j}\frac{R_\mathrm{D}}{L_\mathrm{D}}\right)}\right\} - \mathrm{j}\frac{G}{\omega\Delta_\mathrm{e}} \\ &\doteq \varepsilon_0\varepsilon_{\mathrm{r},\infty}\left\{1 - \frac{\omega_\mathrm{D}^2}{\omega\left(\omega - \mathrm{j}\Omega_\mathrm{D}\right)}\right\} - \mathrm{j}\frac{\sigma_\mathrm{e}}{\omega}\end{aligned} \tag{22}$$

$$\mu_{\text{non-disp}} = \frac{Z_{\text{non-disp}}}{\mathrm{j}\omega\Delta_\mathrm{m}} = \frac{\mathrm{L}}{\Delta_\mathrm{m}} \doteq \mu_0 \tag{23}$$

where ω_D is the resonance frequency of the parallel $L_\mathrm{D} - C$ tank circuit, and Ω_D is the loss factor (reciprocal of the

[d]The artificial subcell with the form factor $\Delta_{\mathrm{e},d}$ is located around the e-node where E_d is sampled.

[e]The artificial subcell with its form factor $\Delta_{\mathrm{m},d}$ is located around the h-node where H_d is sampled.

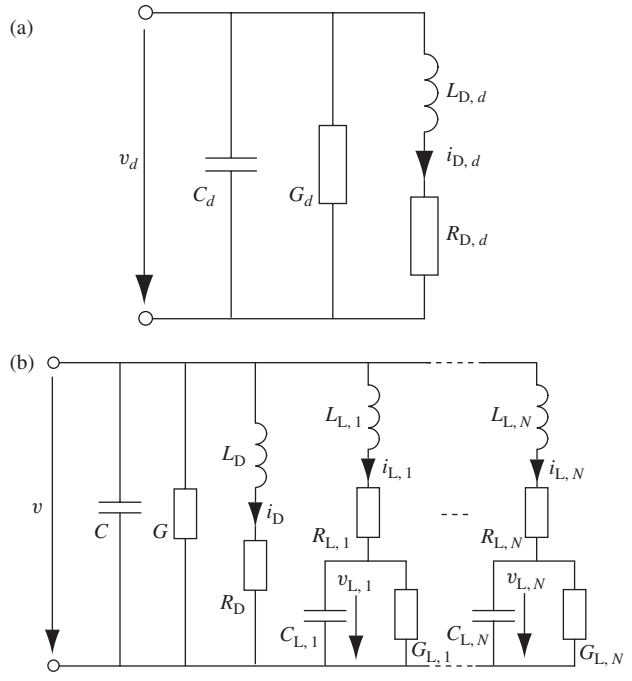

Fig. 5. Proposed EC models for the permittivity of plasmonic lossy metals. (a) Extended-Drude model ($\tilde{\varepsilon}_{\text{Drude}}$) with the EC admittance Y_{Drude} given by Eq. (22). (b) Combined Drude/N-Pole-Lorentz model ($\tilde{\varepsilon}_{\text{D+L}}$) with the EC admittance $Y_{\text{D+L}}$ given by Eq. (30). Here the direction indices d have been omitted for better readability.

relaxation time $\tau_{\text{D}} = L_{\text{D}}/R_{\text{D}}$) of the series $L_{\text{D}} - R_{\text{D}}$ circuit, and from which the plasma frequency of the Drude model $\omega_{\text{p, Drude}}$(where $\Re\{\tilde{\varepsilon}_{\text{Drude}}\} = 0$) follows as

$$\omega_{\text{p, Drude}}^2 = \omega_{\text{D}}^2 - \Omega_{\text{D}}^2 \tag{24}$$

The parameter $\varepsilon_{\text{r},\infty}$ is the relative permittivity at $f \to \infty$, which strictly has to be 1 in the limit but may be used as a free parameter in a frequency-limited band for optimal fitting to experimental data. The parameter σ_{e} is usually not present in the classical Drude model, hence the terminology *extended Drude*, but it was found to improve the fitting to measured losses. Figure 6 plots the complex permittivity $\tilde{\varepsilon}_{\text{Drude}}$ of Eq. (22) for the data $\varepsilon_{\text{r},\infty} = 3.94, \omega_{\text{D}} = 7.01 \times 10^{15}$ rad/s, $\Omega_{\text{D}} = 2.30 \times 10^{13}$ rad/s and $\sigma_{\text{e}} = 7.97 \times 10^3$ S/m, which are used in Section 3.3 to fit measured data of silver (Ag).[12] For comparison, the lossless case $\Omega_{\text{D}} = 0.0$ rad/s and $\sigma_{\text{e}} = 0.0$ S/m is also represented.

Due to the additional energy storage, induced by L_{D}, compared to the non-dispersive case, the time-continuous Ampere's circuit law of Eq. (13) is extended, from the Kirchhoff's current law in Figure 5(a), to the system

$$\left\{1 - \text{S}_{d+1}^{-1}\right\} i_{d+2} - \left\{1 - \text{S}_{d+2}^{-1}\right\} i_{d+1} + i_{\text{src},d} = +C_d \frac{\text{d}}{\text{d}t} v_d + G_d v_d + i_{\text{D},d} \tag{25}$$

$$v_d = +L_{\text{D},d} \frac{\text{d}}{\text{d}t} i_{\text{D},d} + R_{\text{D},d} i_{\text{D},d} \tag{26}$$

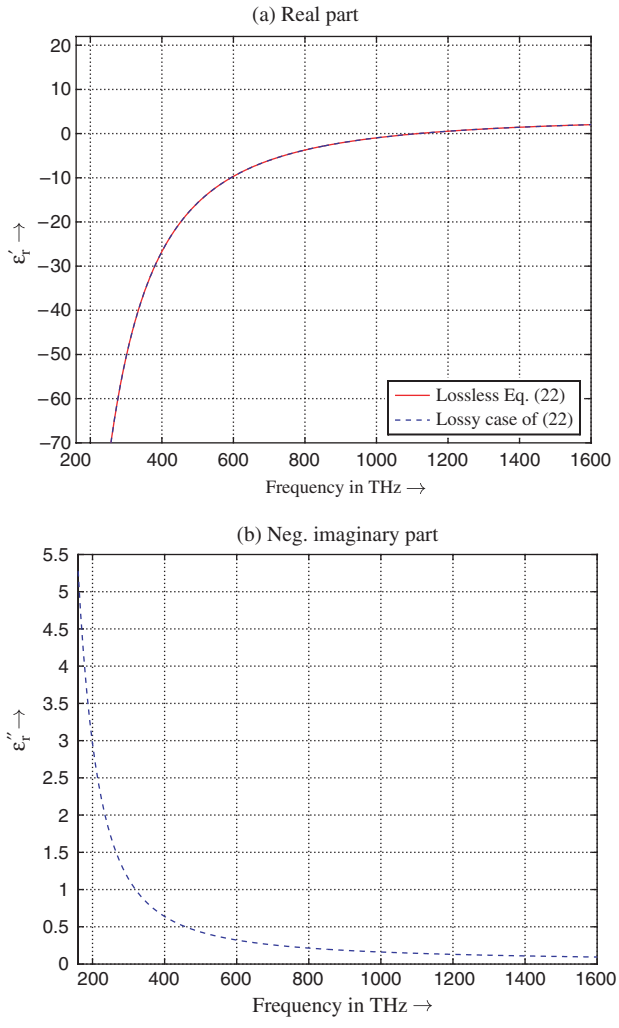

Fig. 6. Extended Drude model complex permittivity $\tilde{\varepsilon}_{\text{Drude}} = \tilde{\varepsilon}'_{\text{Drude}} - \text{j}\tilde{\varepsilon}''_{\text{Drude}}$ as a function of frequency for the lossless and lossy case of Eq. (22).

The final update equations representing the extended Drude counterpart of Eq. (17) are obtained as

$$v_d^n = \frac{1 - \frac{\Delta t G_d}{2C_d}}{1 + \frac{\Delta t G_d}{2C_d}} v_d^{n-1} + \frac{\Delta t}{C_d} \frac{\left\{1 - \text{S}_{d+1}^{-1}\right\} i_{d+2}^{n-1/2} - \left\{1 - \text{S}_{d+2}^{-1}\right\} i_{d+1}^{n-1/2} - i_{\text{D},d}^{n-1/2} + i_{\text{src},d}^{n-1/2}}{1 + \frac{\Delta t G_d}{2C_d}} \tag{27}$$

$$i_{\text{D},d}^{n+1/2} = \frac{1 - \frac{\Delta t R_{\text{D},d}}{2L_{\text{D},d}}}{1 + \frac{\Delta t R_{\text{D},d}}{2L_{\text{D},d}}} i_{\text{D},d}^{n-1/2} + \frac{\Delta t}{L_{\text{D},d}} \frac{v_d^n}{1 + \frac{\Delta t R_{\text{D},d}}{2L_{\text{D},d}}} \tag{28}$$

The extended Drude update scheme given in Eqs. (27), (28) and (18) may be shown[10] to follow the stability criterion

$$\Delta t_{\text{Drude}} < \frac{2}{\max_{X \in \Omega, d \in \{0,1,2\}} \sqrt{\frac{1}{C_d}\left(\frac{1}{L_{\text{D},d}} + \frac{4}{L_{d+1}} + \frac{4}{S_{d+2}^{-1} L_{d+1}} + \frac{4}{L_{d+2}} + \frac{4}{S_{d+1}^{-1} L_{d+2}}\right)}}$$

$$\doteq \frac{2}{\max_{\boldsymbol{X}\in\Omega,\, d\in\{0,1,2\}} \omega_{\mathrm{Drude},\,d}}$$

$$= \frac{2}{\max_{\boldsymbol{X}\in\Omega,\, d\in\{0,1,2\}} \sqrt{\omega^2_{\mathrm{non\text{-}disp},\,d} + \frac{1}{L_{\mathrm{D},\,d} C_d}}} \tag{29}$$

Equation (29) is more restrictive than the non-dispersive case criterion $[\Delta t_{\mathrm{Drude}} < \Delta t_{\mathrm{non\text{-}disp}}]$ due to the additional term $1/L_{\mathrm{D},\,d}$, which introduces the dispersion. In Ref. [10] stability criteria for dispersive materials have been derived within the framework of EC FDTD, while the CFL criterion[6] was derived for non-dispersive materials. Therefore the later can not guarantee a stable time iteration in the presence of dispersion.

3.2. Combined Drude/*N*-Pole-Lorentz EC Model

As will be shown in Section 3.3, the *extended Drude* model presented in Section 3.1 is valid only up to the surface plasmon resonance frequency ω_{sp}, which is equal to 843 THz for an Ag–SiO_2 interface. If the plasmonic devices to be simulated operate above the surface plasmon resonance frequency a more sophisticated EC model is required, including additional Lorentz terms to account for bound electron resonances.[3] In this case, the Drude EC admittance Y_{Drude} depicted in Figure 5(a) is extended by one or several LC series resonators, including an inductance $L_{\mathrm{L},\,p}$ with a series resistance $R_{\mathrm{L},\,p}$ and a capacitance $C_{\mathrm{L},\,p}$ with a conductance $G_{\mathrm{L},\,p}$ in parallel, as shown in Figure 5(b). The permittivity in Eq. (20) becomes then

$$\tilde{\varepsilon}_{\mathrm{D+L}} = \frac{Y_{\mathrm{D+L}}}{\mathrm{j}\omega\Delta_{\mathrm{e}}}$$

$$= \frac{C}{\Delta_{\mathrm{e}}}\left\{1 - \frac{\frac{1}{L_{\mathrm{DC}}}}{\omega\left(\omega - \mathrm{j}\frac{R_{\mathrm{D}}}{L_{\mathrm{D}}}\right)} - \sum_{p=1}^{N} \frac{\frac{1}{L_{\mathrm{L},\,p}} C\left(1 - \mathrm{j}\frac{G_{\mathrm{L},\,p}}{\omega C_{\mathrm{L},\,p}}\right)}{\omega^2 - \frac{1}{L_{\mathrm{L},\,p} C_{\mathrm{L},\,p}}\left(1 + R_{\mathrm{L},\,p} G_{\mathrm{L},\,p}\right) - \mathrm{j}\omega\left(\frac{R_{\mathrm{L},\,p}}{L_{\mathrm{L},\,p}} + \frac{G_{\mathrm{L},\,p}}{C_{\mathrm{L},\,p}}\right)}\right\} - \mathrm{j}\frac{G}{\omega\Delta_{\mathrm{e}}}$$

$$\doteq \varepsilon_0\varepsilon_{\mathrm{r},\infty}\left\{1 - \frac{\omega^2_{\mathrm{D}}}{\omega\left(\omega - \mathrm{j}\Omega_{\mathrm{D}}\right)} - \sum_{p=1}^{N} \frac{\omega^2_{\mathrm{L},\,p}\left(1 - \mathrm{j}\frac{\Omega_{\mathrm{sh},\,p}}{\omega}\right)}{\omega^2 - \omega^2_{0,\,p} - \mathrm{j}\omega\left(\Omega_{\mathrm{se},\,p} + \Omega_{\mathrm{sh},\,p}\right)}\right\} - \mathrm{j}\frac{\sigma_{\mathrm{e}}}{\omega} \tag{30}$$

where the same comments as in Eq. (22) apply to $\varepsilon_{\mathrm{r},\infty}$, ω_{D}, Ω_{D} and σ_{e}. $\omega_{0,\,p}$ is the resonance frequency of the $L_{\mathrm{L},\,p} - C_{\mathrm{L},\,p}$ series circuit, and $\Omega_{\mathrm{se},\,p}$ and $\Omega_{\mathrm{sh},\,p}$ are the loss factors (reciprocal of the relaxation time τ) of the $L_{\mathrm{L},\,p} - R_{\mathrm{L},\,p}$ series and the $C_{\mathrm{L},\,p} - G_{\mathrm{L},\,p}$ shunt circuit, respectively. The parameter $\Omega_{\mathrm{sh},\,p}$ is usually not present in a combined Drude/Lorentz model (as the parameter σ_{e} for the extended Drude model) but might be useful to fit experimental data, especially the losses.

This type of dispersive and lossy behavior (with at least one pole and one zero in the real part of the frequency dependant material parameters) may also be encountered in other cases, such as metamaterial transmission lines,[13] split ring resonator metamaterial structures,[14] and ferrimagnetic or ferromagnetic materials.[15]

Figure 7 plots the combined Drude/1-pole-Lorentz complex permittivity $\tilde{\varepsilon}_{\mathrm{D+L}}$ for the data $\varepsilon_{\mathrm{r},\infty} = 1.138, \omega_{\mathrm{D}} = 1.30 \times 10^{16}$ rad/s, $\Omega_{\mathrm{D}} = 2.585 \times 10^{13}$ rad/s, $\omega_{0,\,1} = 7.5 \times 10^{15}$ rad/s, $\Omega_{\mathrm{se},\,1} = 3.0 \times 10^{14}$ rad/s, $\Omega_{\mathrm{sh},\,1} = 0.0$ rad/s, $\omega_{\mathrm{L},\,1} = 9.6075 \times 10^{15}$ rad/s, $\sigma_{\mathrm{e}} = 4.035 \times 10^{3}$ S/m, which are used in Section 3.3 to fit experimental data [12] for silver (Ag). For comparison, the lossless case $\Omega_{\mathrm{D}} = 0.0$ rad/s, $\Omega_{\mathrm{se},\,1} = 0.0$ rad/s, $\Omega_{\mathrm{sh},\,1} = 0.0$ rad/s and $\sigma_{\mathrm{e}} = 0.0$ S/m is also represented.

Due to the additional energy storages, induced by L_{D}, $L_{\mathrm{L},\,p}, C_{\mathrm{D},\,p}$, compared to the non-dispersive case, the time-continuous Ampere's circuit law of Eq. (13) is extended,

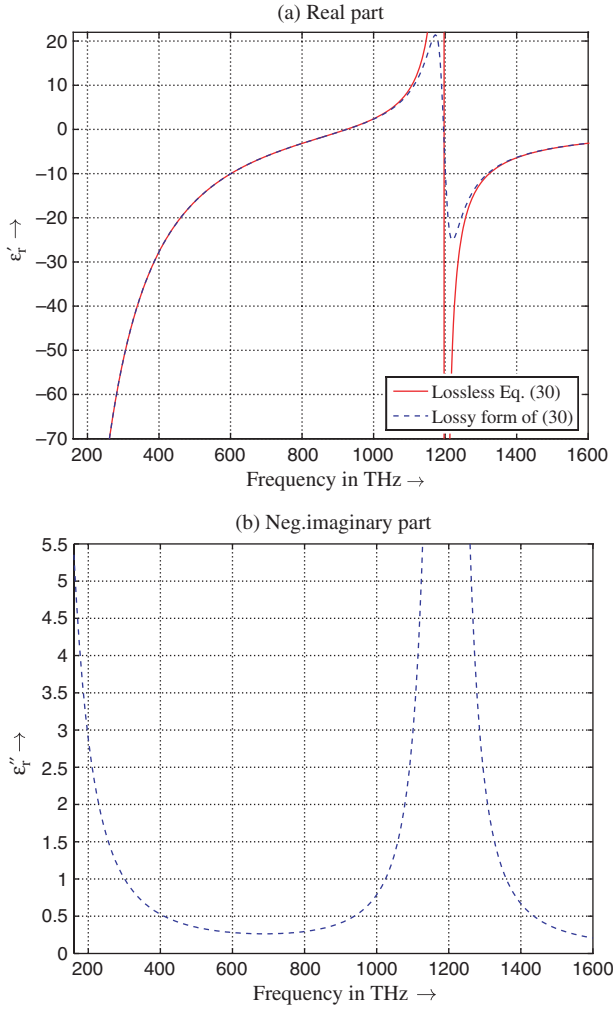

Fig. 7. Combined Drude/1-Pole-Lorentz complex permittivity $\tilde{\varepsilon}_{\mathrm{D+L}} = \tilde{\varepsilon}'_{\mathrm{D+L}} - \mathrm{j}\tilde{\varepsilon}''_{\mathrm{D+L}}$ as a function of frequency for the lossless and lossy case of Eq. (30).

from the Kirchhoff's current law in Figure 5(b), to the system

$$\left\{1-\mathrm{S}_{d+1}^{-1}\right\}i_{d+2}-\left\{1-\mathrm{S}_{d+2}^{-1}\right\}i_{d+1}+i_{\mathrm{src},d} =+C_d\frac{\mathrm{d}}{\mathrm{d}t}v_d+G_d v_d+i_{\mathrm{D},d}+\sum_{p=1}^{N}i_{\mathrm{L},p,d} \quad (31)$$

$$v_d=+L_{\mathrm{D},d}\frac{\mathrm{d}}{\mathrm{d}t}i_{\mathrm{D},d}+R_{\mathrm{D},d}i_{\mathrm{D},d} \quad (32)$$

$$v_d=+L_{\mathrm{L},p,d}\frac{\mathrm{d}}{\mathrm{d}t}i_{\mathrm{L},p,d}+R_{\mathrm{L},p,d}i_{\mathrm{L},p,d}+v_{\mathrm{L},p,d} \quad \forall p\in\{1,\ldots,N\} \quad (33)$$

$$i_{\mathrm{L},p,d}=+C_{\mathrm{L},p,d}\frac{\mathrm{d}}{\mathrm{d}t}v_{\mathrm{L},p,d}+G_{\mathrm{L},p,d}\times v_{\mathrm{L},p,d} \quad \forall p\in\{1,\ldots,N\} \quad (34)$$

The final update equations representing the combined Drude/N-pole Lorentz counterpart of Eq. (17) are obtained by replacing the continuous time derivatives by central finite differences

$$\left\{1-\mathrm{S}_{d+1}^{-1}\right\}i_{d+2}^{n-1/2}-\left\{1-\mathrm{S}_{d+2}^{-1}\right\}i_{d+1}^{n-1/2}+i_{\mathrm{src},d}^{n-1/2} =+C_d\frac{v_d^n-v_d^{n-1}}{\Delta t}+G_d\frac{v_d^n+v_d^{n-1}}{2}+i_{\mathrm{D},d}^{n-1/2}+\sum_{p=1}^{N}i_{\mathrm{L},p,d}^{n-1/2} \quad (35)$$

$$v_d^n=+L_{\mathrm{D},d}\frac{i_{\mathrm{D},d}^{n+1/2}-i_{\mathrm{D},d}^{n-1/2}}{\Delta t}+R_{\mathrm{D},d}\frac{i_{\mathrm{D},d}^{n+1/2}-i_{\mathrm{D},d}^{n-1/2}}{2} \quad (36)$$

$$v_d^n=+L_{\mathrm{L},p,d}\frac{i_{\mathrm{L},p,d}^{n+1/2}-i_{\mathrm{L},p,d}^{n-1/2}}{\Delta t}+R_{\mathrm{L},p,d}\frac{i_{\mathrm{L},p,d}^{n+1/2}-i_{\mathrm{L},p,d}^{n-1/2}}{2}+v_{\mathrm{L},p,d}^n \quad \forall p \quad (37)$$

$$i_{\mathrm{L},p,d}^{n-1/2}=+C_{\mathrm{L},p,d}\frac{v_{\mathrm{L},p,d}^n-v_{\mathrm{L},p,d}^{n-1}}{\Delta t}+G_{\mathrm{L},p,d}\frac{v_{\mathrm{L},p,d}^n+v_{\mathrm{L},p,d}^{n-1}}{2} \quad \forall p \quad (38)$$

and are given finally as

$$v_d^n=\frac{1-\frac{\Delta t G_d}{2C_d}}{1+\frac{\Delta t G_d}{2C_d}}v_d^{n-1}+\frac{\Delta t}{C_d}\frac{\left\{1-\mathrm{S}_{d+1}^{-1}\right\}i_{d+2}^{n-1/2}-\left\{1-\mathrm{S}_{d+2}^{-1}\right\}i_{d+1}^{n-1/2}-i_{\mathrm{D},d}^{n-1/2}-\sum_{p=1}^{N}i_{\mathrm{L},p,d}^{n-1/2}+i_{\mathrm{src},d}^{n-1/2}}{1+\frac{\Delta t G_d}{2C_d}} \quad (39)$$

$$i_{\mathrm{D},d}^{n+1/2}=\frac{1-\frac{\Delta t R_{\mathrm{D},d}}{2L_{\mathrm{D},d}}}{1+\frac{\Delta t R_{\mathrm{D},d}}{2L_{\mathrm{D},d}}}i_{\mathrm{D},d}^{n-1/2}+\frac{\Delta t}{L_{\mathrm{D},d}}\frac{v_d^n}{1+\frac{\Delta t R_{\mathrm{D},d}}{2L_{\mathrm{D},d}}} \quad (40)$$

$$i_{\mathrm{L},p,d}^{n+1/2}=\frac{1-\frac{\Delta t R_{\mathrm{L},p,d}}{2L_{\mathrm{L},p,d}}}{1+\frac{\Delta t R_{\mathrm{L},p,d}}{2L_{\mathrm{L},p,d}}}i_{\mathrm{L},p,d}^{n-1/2}+\frac{\Delta t}{L_{\mathrm{L},p,d}}\frac{v_d^n-v_{\mathrm{L},p,d}^n}{1+\frac{\Delta t R_{\mathrm{L},p,d}}{2L_{\mathrm{L},p,d}}} \quad \forall p\in\{1,\ldots,N\} \quad (41)$$

$$v_{\mathrm{L},p,d}^n=\frac{1-\frac{\Delta t G_{\mathrm{L},p,d}}{2C_{\mathrm{L},p,d}}}{1+\frac{\Delta t G_{\mathrm{L},p,d}}{2C_{\mathrm{L},p,d}}}v_{\mathrm{L},p,d}^{n-1}+\frac{\Delta t}{C_{\mathrm{L},p,d}}\frac{i_d^{n-1/2}}{1+\frac{\Delta t G_{\mathrm{L},p,d}}{2C_{\mathrm{L},p,d}}} \quad \forall p\in\{1,\ldots,N\} \quad (42)$$

The stability criterion of this system for the interesting case of $N=1$ (in the rest of the section $p=N=1$ is omitted for better readability) can be derived following the approach presented in Ref. [10] and reads

$$\Delta t_{\mathrm{D+L}}<\frac{2}{\max_{\boldsymbol{X}\in\Omega,d\in\{0,1,2\}}\sqrt{\omega_{\mathrm{Drude},d}^2+\omega_{0,d}^2+\omega_{\mathrm{L},d}^2}}<\frac{2}{\max_{\boldsymbol{X}\in\Omega,d\in\{0,1,2\}}\omega_{\mathrm{D+L},d}} \quad (43)$$

with

$$\omega_{\mathrm{D+L},d}^2 \doteq\frac{1}{2}\left\{\omega_{\mathrm{Drude},d}^2+\omega_{0,d}^2+\omega_{\mathrm{L},d}^2+\sqrt{\omega_{\mathrm{Drude},d}^4+\omega_{0,d}^4+\omega_{\mathrm{L},d}^4+2\left(\omega_{\mathrm{Drude},d}^2\omega_{\mathrm{L},d}^2+\omega_{0,d}^2\omega_{\mathrm{L},d}^2-\omega_{\mathrm{Drude},d}^2\omega_{0,d}^2\right)}\right\} <\omega_{\mathrm{Drude},d}^2+\omega_{0,d}^2+\omega_{\mathrm{L},d}^2 \quad (44)$$

where

$$\omega_{0,d}^2\doteq\frac{1}{L_{\mathrm{L},d}C_{\mathrm{L},d}},\quad \omega_{\mathrm{L},d}^2\doteq\frac{1}{L_{\mathrm{L},d}C_d} \quad \text{and} \quad \omega_{\mathrm{Drude},d}^2 \quad \text{already defined in Eq. (29)} \quad (45)$$

The simplified denominator, $\omega_{\mathrm{Drude},d}^2+\omega_{0,d}^2+\omega_{\mathrm{L},d}^2$, in Eq. (43) yields a slightly lower limit for the time step, but is easier to compute. The term is an upper estimate for the complicated $\omega_{\mathrm{D+L},d}$ as given in Eq. (44). Inspection of Eq. (43) reveals that a smaller time step limit must be used compared to the non-dispersive and also the Drude case [$\Delta t_{\mathrm{D+L}}<\Delta t_{\mathrm{Drude}}<\Delta t_{\mathrm{non\text{-}disp}}$], due to two additional terms, $\omega_{0,d}^2+\omega_{\mathrm{L},d}^2$, in the denominator of Eq. (43).

3.3. Comparison of the Proposed EC Models and Curve-Fitting to Measured Permittivities

Figure 8 compares the performances of the extended Drude and combined Drude/1-Pole EC models with experimental data[12] for the complex permittivity frequency function in the case of Ag. The EC model parameters have been obtained by curve fitting in a specific frequency range using the MATLAB curve-fitting toolbox. The experimental curves display a smooth real part $\varepsilon_{\mathrm{r}}'$, which may be perfectly fitted with relatively simple models, but, probably due to measurement uncertainties, a rather irregular imaginary part $\varepsilon_{\mathrm{r}}''$ (especially in the range of 250 to 450 THz), which is more difficult to curve fit.

The extended Drude EC model parameter set [$\varepsilon_{\mathrm{r},\infty}=3.94, \omega_{\mathrm{D}}=7.01\times10^{15}$ rad/s, $\Omega_{\mathrm{D}}=2.30\times10^{13}$ rad/s,

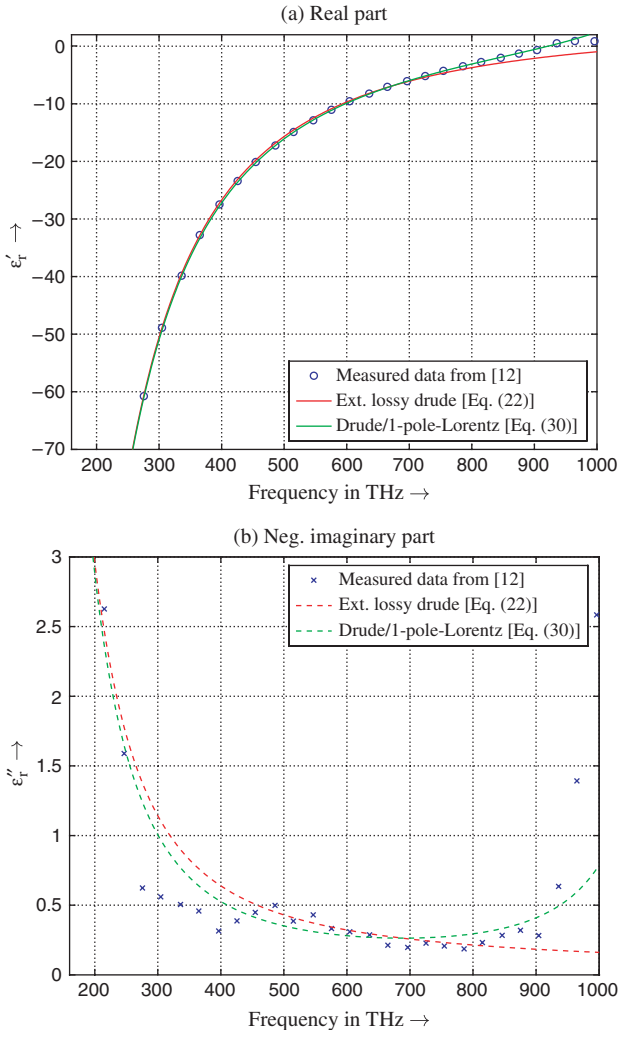

Fig. 8. Measured complex permittivity $\varepsilon_r = \varepsilon'_r - j\varepsilon''_r$ from Ref. [12] compared to the data obtained by a curve-fitted extended Drude model (Eq. (22)) and an optimized combined Drude/1-pole-Lorentz approximation (Eq. (30)).

$\sigma_e = 7.97 \times 10^3$ S/m] provides excellent accuracy for ε'_r throughout the frequency range of 200 to 800 THz (Fig. 8(a)). In contrast, this model overestimates ε''_r from 250 to 450 THz, and underestimates ε''_r above 800 THz. The later is due to the ignored excitation of inner bound electrons.[3]

The combined Drude/1-pole-Lorentz EC model broadens this frequency range of accuracy, as may be seen in Figure 8. In this case, the optimized parameter set [$\varepsilon_{r,\infty} = 1.138, \omega_D = 1.30 \times 10^{16}$ rad/s, $\Omega_D = 2.585 \times 10^{13}$ rad/s, $\omega_{0,1} = 7.5 \times 10^{15}$ rad/s, $\Omega_{se,1} = 3.0 \times 10^{14}$ rad/s, $\Omega_{sh,1} = 0.0$ rad/s, $\omega_{L,1} = 9.6075 \times 10^{15}$ rad/s, $\sigma_e = 4.035 \times 10^3$ S/m] improves the accuracy of ε'_r beyond 800 THz (Fig. 8(a)), and the accuracy of ε''_r below 450 THz and above 800 THz (where intraband transitions of bound electrons are now accounted for by the Lorentz pole).

The coupler presented in the next section operates in the range of 250 to 650 THz (corresponds to the wavelength range of 1200 nm down to 460 nm), where the extended Drude model is accurate enough and will be therefore the one to be used.

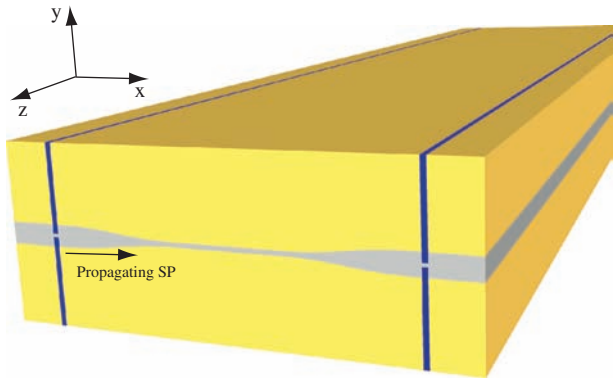

Fig. 9. Perspective view of the coupled-SP codirectional nano-coupler. The tapered Ag film (gray) is embedded in SiO_2 (yellow). The coupled waves propagate along the x direction. The blue lines indicate the locations of the 4 ports (approximate size of the penetration depth in the FDTD analysis) used in the scattering parameter computations.

4. NOVEL CO-DIRECTIONAL COUPLED-SP NANO-SCALE COUPLER

A novel optical coupled-SP power splitter[f] (single operation frequency of 685 THz) featuring an extremely small *nano-scale* size was presented in Ref. [16]. The general configuration of the device is shown in Figure 9. This structure is here investigated over a broader bandwidth (250 to 650 THz), its geometry is optimized for various modes of operation (splitter functionality at three frequencies $f_{1,3,5}$ and diplexer operation for four frequency bands around $f_{0,2,4,6}$) and practical use (e.g., the device has been designed for diplex operation at the two wavelength $\lambda_2 =$ 633 nm [red] and $\lambda_4 = 533$ nm [green], where laser sources (He-Ne, Nd-YAG) exist. This optimized geometry is specified in Figure 10. The device consists of a metallic Ag film tapered to a small width in its center and embedded within SiO_2 ($\varepsilon_{SiO_2} = 2.09$).

A SP excited by a laser source at one Ag–SiO_2 interface (port 1) propagates along the structure and couples energy to the other interface in the narrow Ag region where its field overlaps both interfaces. By proper design of the narrow-coupling region width and length, arbitrary levels of signal may be transmitted to the *coupled* output (port 4), while the remaining power is guided toward the *through* output (port 3). The fourth output (port 2) is always isolated. A fundamental difference between this and other more conventional SP couplers[4,5] is that this coupler operates in *single-interface* (SI) waveguiding mode. In addition, this coupler exhibits substantially smaller size

[f] Patent Pending.

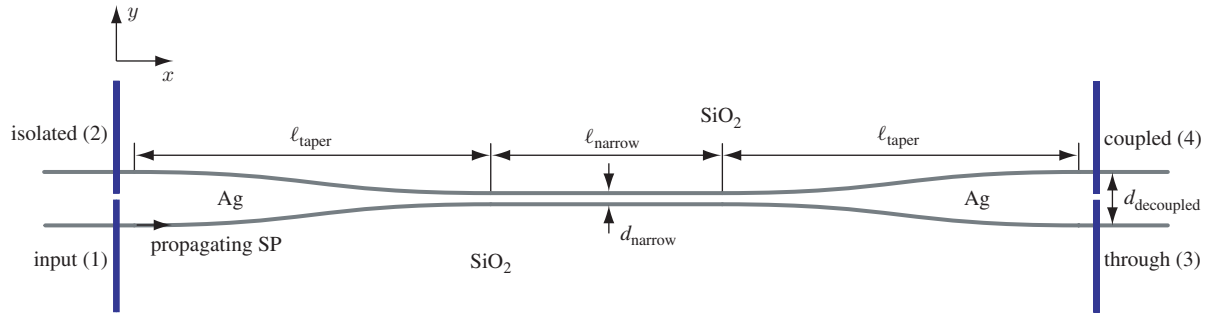

Fig. 10. Longitudinal cross section of the (xy cut) of the nano-coupler of Figure 9 with relevant design parameters. The optimized parameter values are: $d_{narrow}=25$ nm, $d_{decoupled}=120$ nm, $\ell_{narrow}=520$ nm, $\ell_{taper}=800$ nm. The narrow section ℓ_{narrow} is sub-wavelength compared to the free-space wavelength λ_0 at $f_2=475$ THz of 632 nm.

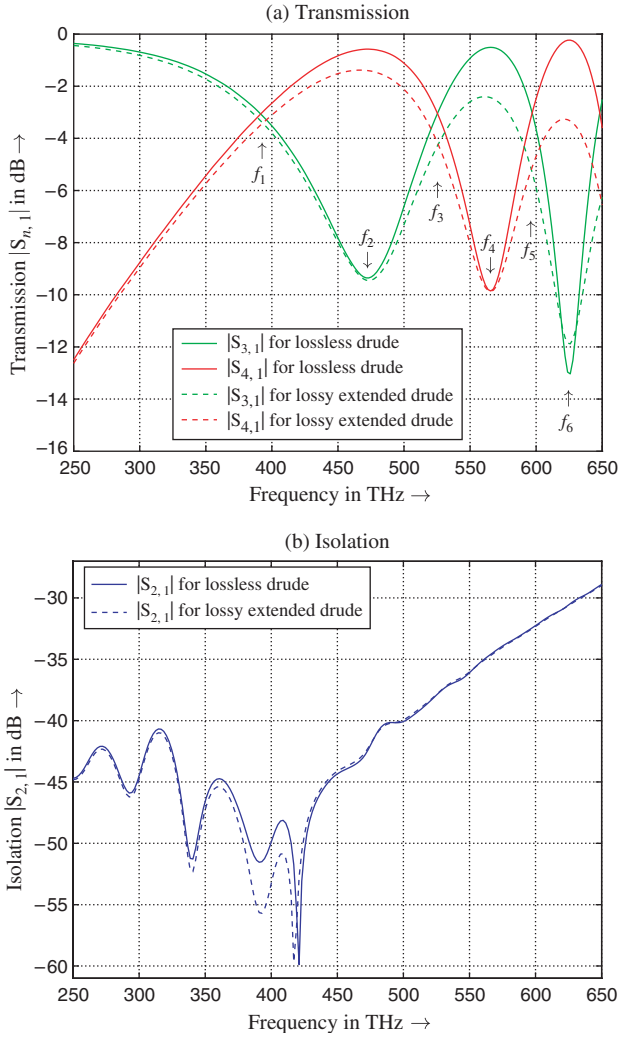

Fig. 11. Full-wave simulated scattering parameters of the coupler depicted in Figures 9 and 10 using the lossless and lossy extended Drude model of Eq. (22). At $f_1=390$ THz ($\lambda_1=769$ nm), $f_3=525$ THz ($\lambda_3=571$ nm) and $f_5=596$ THz ($\lambda_5=503$ nm) the device operates as 90° hybrid power splitter, while at $f_0=250$ THz ($\lambda_0=1200$ nm), $f_2=475$ THz ($\lambda_2=633$ nm), $f_4=563$ THz ($\lambda_4=533$ nm) and $f_6=624$ THz ($\lambda_6=480$ nm) it may be used as a diplexer.

(the mentioned film-guided long-range SP coupler have a length of several mm!). Here we present the results of this SI-guided SP coupler generated with the proposed EC FDTD technique of Section 2.3 and using the extended-Drude dispersive model of Section 3.

The Ag–SiO_2 interface supports a single propagating mode, as required for the coupler operation, in the range of 200 to 800 THz. The $1/e$-propagation lengths of the SP interface waveguides (8.7 dB signal decay) at 200, 400, 600 and 800 THz are 734, 161, 11.35 and 0.36 μm, respectively; this means that, assuming a typical overall device length (including the taper sections) of 2 μm, the coupler may be used with reasonable loss up to around 600 THz. The lower frequency limit is fixed by reduction of field confinement far from the SP resonance; below 400 THz, the modes become relatively loosely bound to the interface, with wide penetration into the dielectric, and may easily leak out of the structure if the interface is not smooth. Especially at the taper sections low frequency leakage can occur, if the shape of the taper is not smooth enough.

The scattering parameters of the coupled-SP nano-scale coupler are shown in Figure 11. Depending on the frequency bands chosen (as indicated in the caption of the figure), the device may be operated either as a 90° *hybrid power splitter* or as a *diplexer*. Exact design formulas based on rigorous coupled mode theory are currently being developed by the authors.

The results reveal that the triband power splitter exhibits 0.4, 1.2 and 2.2 dB loss at the frequencies f_1, f_2 and f_3, respectively, while for the diplexer operation at the frequencies f_2, f_4 and f_6 the device exhibits only 1.4, 2.4 dB and 3.2 dB losses. The isolation of ports 3 and 4 in

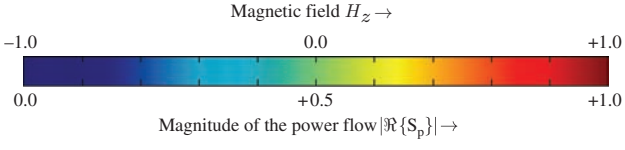

Fig. 12. Legends/scales for normalized fields of the next figures.

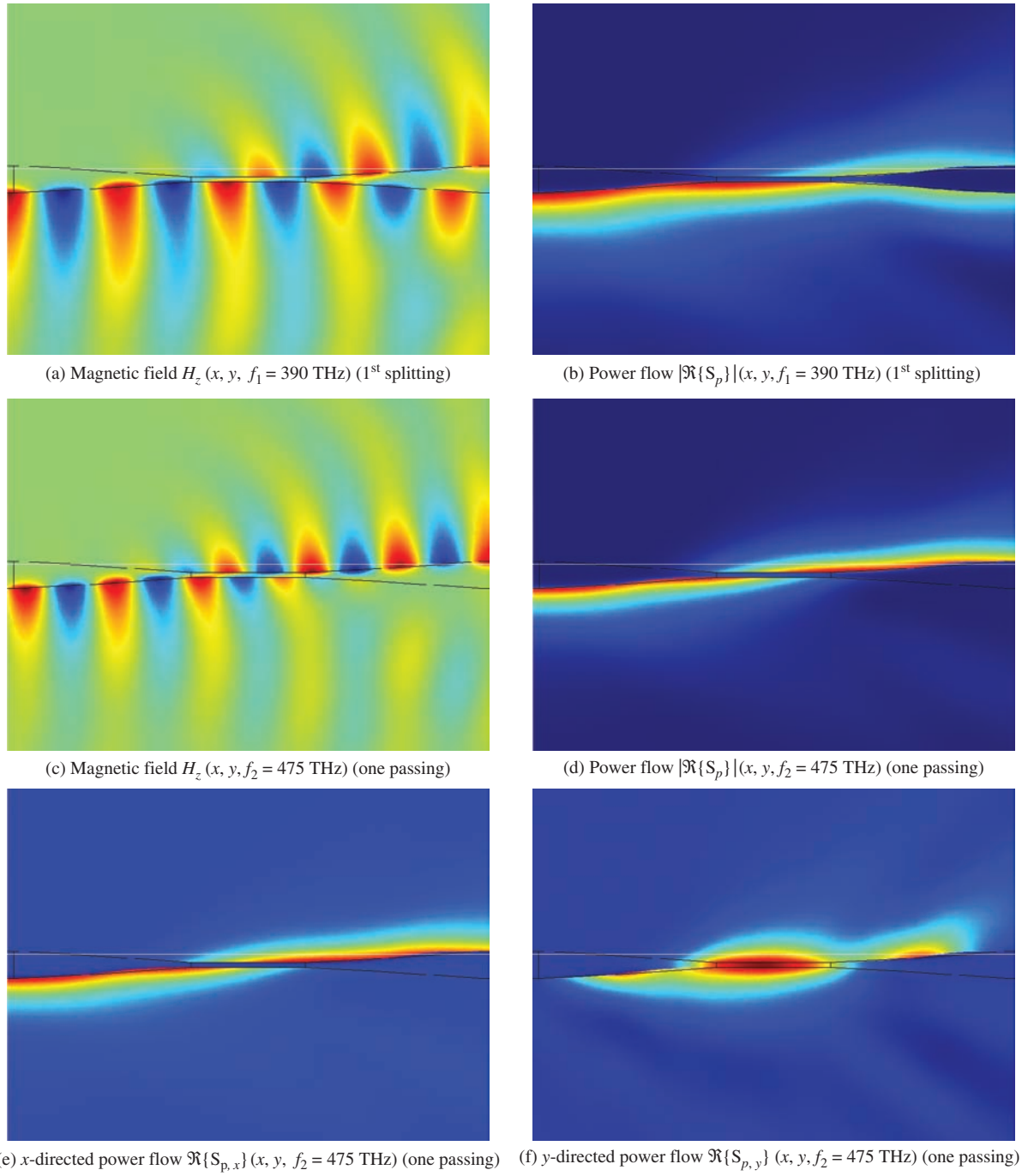

(a) Magnetic field H_z $(x, y, f_1 = 390$ THz) (1^{st} splitting)

(b) Power flow $|\Re\{S_p\}|(x, y, f_1 = 390$ THz) (1^{st} splitting)

(c) Magnetic field H_z $(x, y, f_2 = 475$ THz) (one passing)

(d) Power flow $|\Re\{S_p\}|(x, y, f_2 = 475$ THz) (one passing)

(e) x-directed power flow $\Re\{S_{p,x}\}$ $(x, y, f_2 = 475$ THz) (one passing)

(f) y-directed power flow $\Re\{S_{p,y}\}$ $(x, y, f_2 = 475$ THz) (one passing)

Fig. 13. Normalized fields at the frequency $f_1 = 390$ THz where the incoming power is equally divided to the two coupled ports [(a), (b)] and at the frequency $f_2 = 475$ THz where the incoming wave is fully coupled to the upper Ag/SiO_2 interface [(c), (d)]. The smallest field confinement at the SP interfaces is observed at the lowest frequency, and this confinement increases then monotonically with increasing frequency. In (e) and (f) the x- and y-component of the time-averaged power flow is plotted separately by using two different scales to allow visibility of the the y-directed power flow.

the later diplexing mode is around 10 dB. This parameter needs to be improved in future designs of such plasmonic couplers. The isolation of port 2 (isolated port) should be sufficient for most applications. The coupling to this port is better than −30 dB for all simulated frequencies.

The alternation rate of the coupling to ports 3 and 4, instead of being constant as in a non-dispersive typical dielectric coupler, is increasing progressively as frequency increases, as a result of the guided wavelength compression occurring toward the SP resonance. The lossless-case results suggest higher coupling levels with increased frequency due to increased field confinement and subsequent reduced energy leakage at the SP taper region interfaces. In fact, the lossy-case results show that the opposite trend is

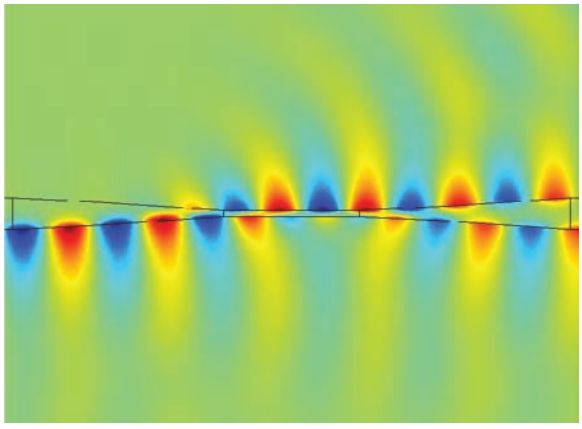

(a) Magnetic field H_z $(x, y, f_3 = 525$ THz) (2^{nd} splitting)

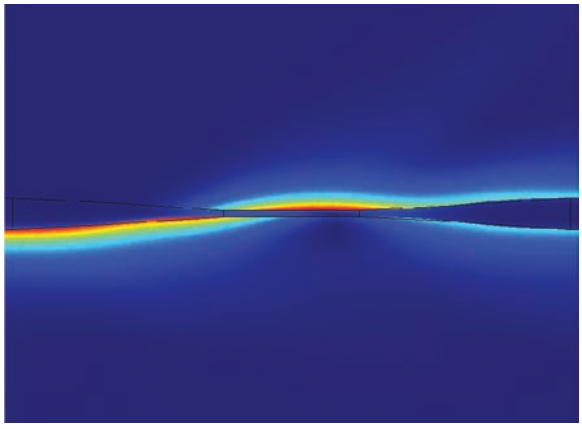

(b) Power flow $|\Re\{S_p\}|(x, y, f_3 = 525$ THz) (2^{nd} splitting)

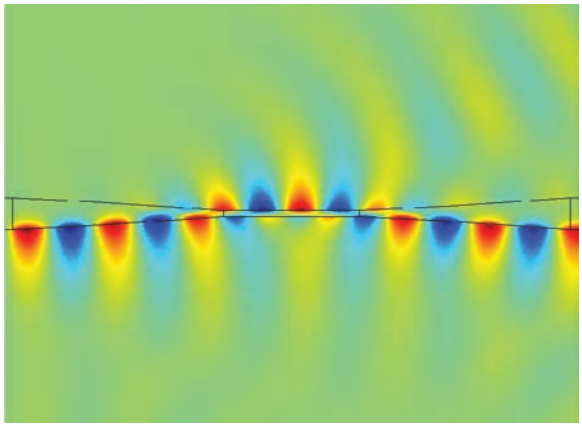

(c) Magnetic field H_z $(x, y, f_4 = 563$ THz) (two passings)

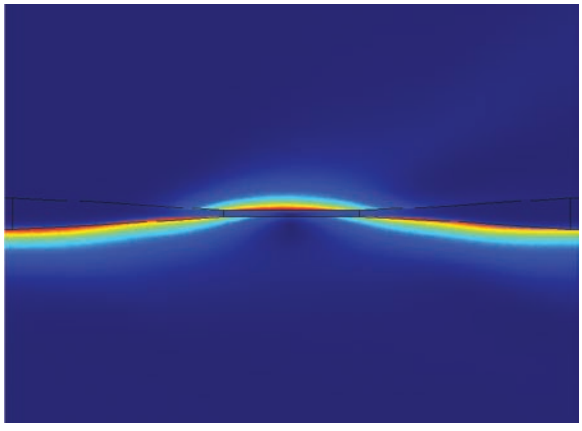

(d) Power flow $|\Re\{S_p\}|(x, y, f_4 = 563$ THz) (two passings)

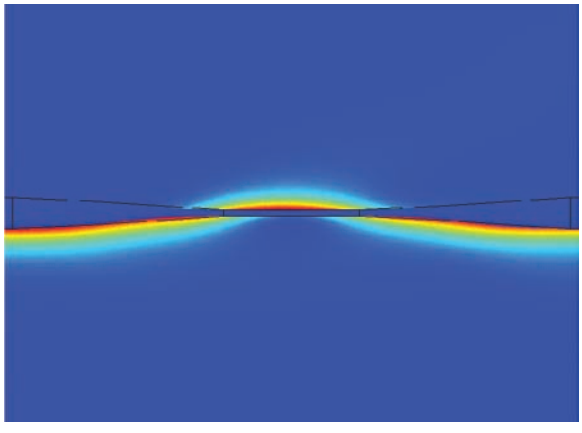

(e) x-directed power flow $\Re\{S_{p,x}\}$ $(x, y, f_4 = 563$ THz) (two passings)

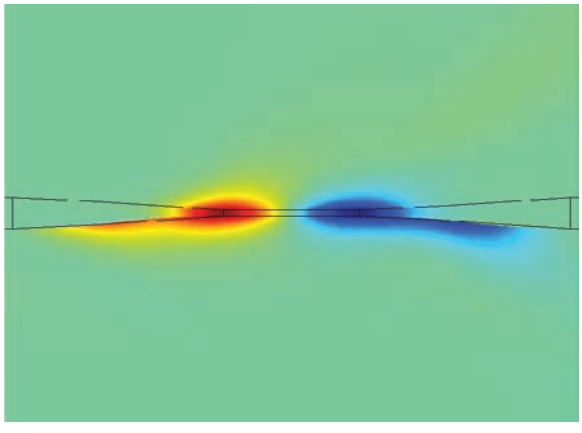

(f) y-directed power flow $\Re\{S_{p,y}\}$ $(x, y, f_4 = 563$ THz) (two passings)

Fig. 14. Normalized fields at the frequency $f_3 = 525$ THz where the incoming power is equally divided to the two coupled ports [(a), (b)] and at the frequency $f_4 = 563$ THz where the incoming wave is fully coupled to the upper Ag/SiO_2 interface and back to the lower one [(c), (d)], and x- and y-component of the time-averaged power flow plotted separately by using two different scales [(e), (f)] to allow visibility of the y-directed power flow.

true; this is explained by the fact that, although the loss of Ag is slightly lower near 650 THz than it is near 475 THz (Fig. 8(b)), the *ratio of* Ag-to-SiO_2 *regions field energies* (with Ag much lossier than SiO_2) increases in a dominant manner as frequency increases, is well be seen next in the field plots.

Finally, with the legends/scales of Figures 12–15 show fields and power distributions in the longitudinal cross section (xy-plane with reference to Fig. 9) of the structure at different frequencies, confirming the scattering parameter results and illustrating the coupling mechanisms described above.

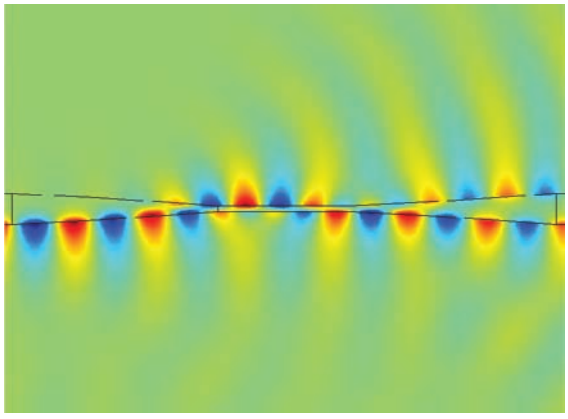

(a) Magnetic field H_z $(x, y, f_5 = 596$ THz) (3^{rd} splitting)

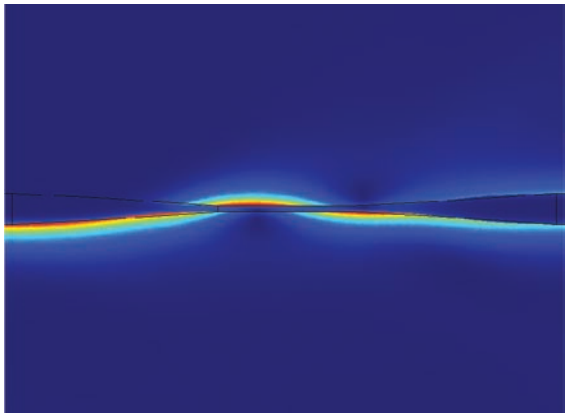

(b) Power flow $|\Re\{S_p\}|(x, y, f_5 = 596$ THz) (3^{rd} splitting)

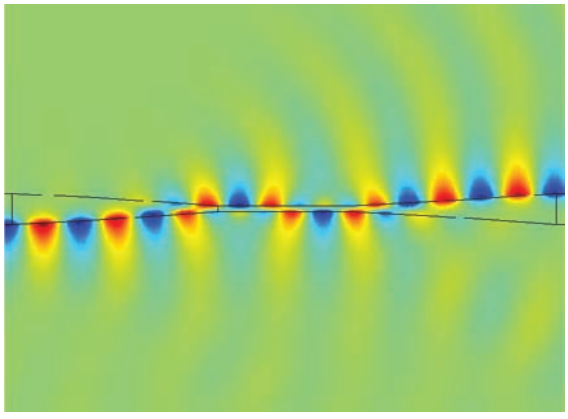

(c) Magnetic field H_z $(x, y, f_6 = 624$ THz) (three passings)

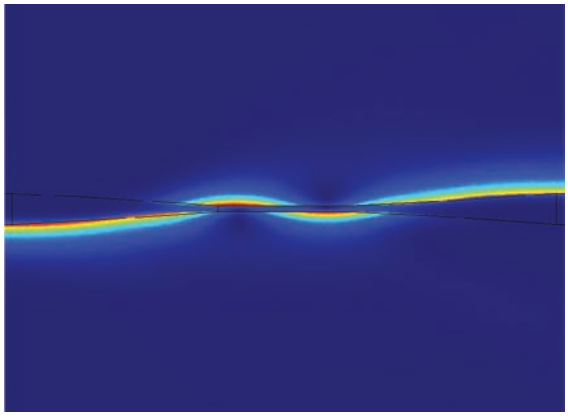

(d) Power flow $|\Re\{S_p\}|(x, y, f_6 = 624$ THz) (three passings)

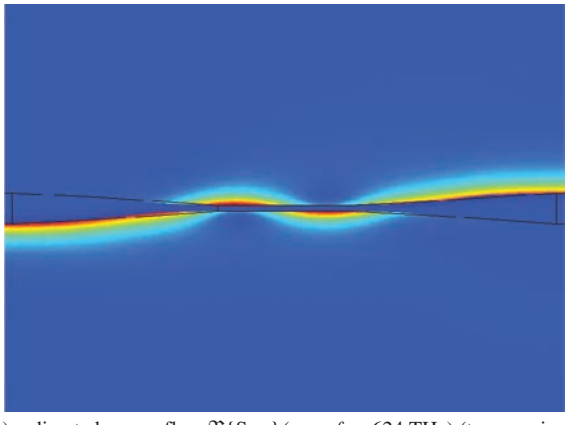

(e) x-directed power flow $\Re\{S_{p,x}\}$ $(x, y, f_6 = 624$ THz) (two passings)

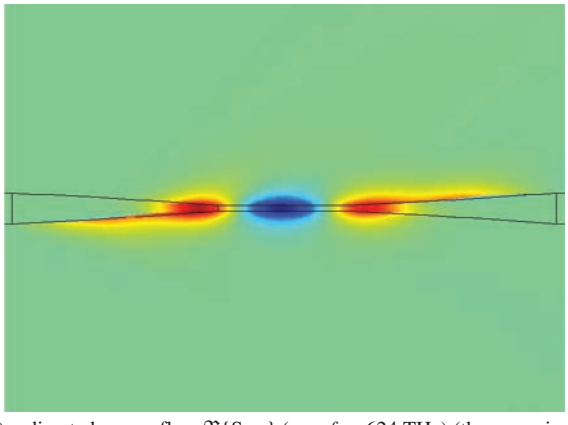

(f) y-directed power flow $\Re\{S_{p,y}\}$ $(x, y, f_6 = 624$ THz) (three passings)

Fig. 15. Normalized fields at the frequency $f_5 = 596$ THz where the incoming power is equally divided to the two coupled ports [(a), (b)] and at the frequency $f_6 = 624$ THz where the incoming wave is fully coupled to the upper Ag/SiO_2 interface, back to the lower one and a third time to the upper interface [(c), (d)], and x- and y-component of the time-averaged power flow plotted separately by using two different scales [(e), (f)] to allow visibility of the y-directed power flow.

5. CONCLUSION

An equivalent circuit (EC) FDTD method has been derived, first for the case of non-dispersive materials and next for the more involved case of dispersive materials. In the later case, both an extended-Drude and a Drude/1-pole Lorentz permittivity function, with corresponding circuit (admittance) models, have been proposed and shown to perfectly agree with experimental data over a wide range of frequencies, with a larger validity range for the second more-sophisticated model.

A novel optical nano-coupler based on SP coupling between two metal-dielectric interfaces of a metal (Ag) slab embedded in a dielectric material (SiO_2) has been proposed, analyzed with the EC FDTD method, characterized in terms of scattering parameters and fields distributions,

and shown to provide several operation modes, including power splitter and diplexer. Due to its super-compact size (around 2 μm) and low-loss (0.4 dB at 769 nm for power splitting operation, and 1.4 dB and 2.4 dB for the diplexing of signals in 633 nm and 533 nm bands) over a broad frequency range (around 250–650 THz), this nano-coupler structure may find various applications in near future.

References

1. E. N. Economou, *Phys. Rev.* 182, 539 **(1969)**.
2. H. Raether, Surface Plasmon on Smooth and Rough Surfaces and on Gratings, Springer, Berlin **(1988)**.
3. L. Novotny and B. Hecht, Principles of Nano-Optics, Cambridge University Press **(2006)**.
4. A. Boltasseva, T. Nikolajsen, K. Leosson, K. Kjaer, M. S. Larsen, and S. I. Bozhevolnyi, *J. Lightwave Tech.* 23, 413 **(2005)**.
5. R. Charbonneau, N. Lahoud, G. Mattiussi, and P. Berini, *Opt. Express* 13, 977 **(2005)**.
6. A. Taflove and S. C. Hagness, Computational Electrodynamics: The Finite-Difference Time-Domain Method, 3rd edn., Artech House, Norwood, MA **(2005)**.
7. D. M. Sullivan, Electromagnetic Simulation Using the FDTD Method, IEEE Press, Piscataway, NJ **(2000)**.
8. A. Rennings, S. Otto, A. Lauer, C. Caloz, and P. Waldow, *Proc. of the European Microwave Association* **(2006)**, Vol. 2, pp. 71–82.
9. A. Rennings, S. Otto, C. Caloz, A. Lauer, W. Bilgic, and P. Waldow, *International Journal of Numerical Modelling* 19, 141 **(2006)**.
10. A. Rennings, C. Caloz, and I. Wolff, *IEEE MTT-S Int. Microwave Symp.,* San Francisco, USA, June **(2006)**, pp. 1069–1072.
11. N. Rouche, P. Habets, and M. Laloy, Stability Theory by Liapunov's Direct Method, Springer, Berlin **(1977)**.
12. P. B. Johnson and R. W. Christy, *Phy. Rev. B* 6, 4370 **(1972)**.
13. A. Rennings, T. Liebig, C. Caloz, and I. Wolff, *IEEE MTT-S Int. Microwave Symp.,* Honolulu, USA, June **(2007)**, pp. 1427–1430.
14. R. A. Shelby, D. R. Smith, and S. Schultz, *Science* 292, 77 **(2001)**.
15. E. M. Lifshitz, L. D. Landau, and L. P. Pitaevskii, Electrodynamics of Continuous Media, 2nd edn., Butterworth-Heinemann, Burlington, MA **(1984)**, Vol. 8.
16. A. Rennings, J. Mosig, S. Gupta, C. Caloz, R. Kashyap, D. Erni, and P. Waldow, *International Symposium on Signals, Systems and Electronics (ISSSE)*, Montréal, Canada, July-August **(2007)**, pp. 471–474.

Received: 26 September 2007. Accepted: 25 October 2007.